CONDENSED MATTER PHYSICS

Electrostatically controlled surface boundary conditions in nematic liquid crystals and colloids

Haridas Mundoor[1], Bohdan Senyuk[1], Mahmoud Almansouri[1], Sungoh Park[1], Blaise Fleury[1], Ivan I. Smalyukh[1,2,3]*

Differing from isotropic fluids, liquid crystals exhibit highly anisotropic interactions with surfaces, which define boundary conditions for the alignment of constituent rod-like molecules at interfaces with colloidal inclusions and confining substrates. We show that surface alignment of the nematic molecules can be controlled by harnessing the competing aligning effects of surface functionalization and electric field arising from surface charging and bulk counterions. The control of ionic content in the bulk and at surfaces allows for tuning orientations of shape-anisotropic particles like platelets within an aligned nematic host and for changing the orientation of director relative to confining substrates. The ensuing anisotropic elastic and electrostatic interactions enable colloidal crystals with reconfigurable symmetries and orientations of inclusions.

INTRODUCTION

From displays to biomedical sensors, applications of liquid crystals (LCs) use monodomain samples created by exploiting anisotropic surface interactions (*1*–*3*). In fundamental studies of LC colloids, surface interactions define the boundary conditions for molecules on particle surfaces and ultimately determine the induced defects and interactions (*4*–*16*). Colloidal assemblies and phases strongly depend on these boundary conditions, which can vary from planar (*9*) to tilted (*8*, *17*) and perpendicular (*4*–*7*), especially for shape-anisotropic particles (*18*–*20*). Surface orientations for the LC's director field $\mathbf{n}(\mathbf{r})$ are determined by the anisotropic part of surface free energy, dubbed "anchoring" energy (*2*, *3*), which, for a given LC, can be controlled through chemical or topographic modification (*7*–*20*), mechanical rubbing (*21*), or photoalignment (*22*). Limitations of controlling surface anchoring hinder the utility of LCs in colloidal assembly and technological applications.

Here, we report the influence of ions on surface anchoring properties, with a focus on defining the behavior of anisotropic colloids dispersed in a nematic LC. We demonstrate a systematic variation of boundary conditions by controlling the ionic content within the LC. We show how it alters equilibrium orientations of charged colloidal particles with respect to the far-field director $\mathbf{n}_0$ and the ensuing self-assembly of colloidal arrays with different crystallographic symmetries.

RESULTS AND DISCUSSION

Platelet-shaped β-$NaYF_4$:Yb,Er particles were synthesized using a modified hydrothermal method (*23*). This chemical synthesis was optimized to yield circular platelets with average diameter $2R \approx 2$ μm and a thickness of 20 nm, as confirmed by scanning electron microscopy (SEM) (Fig. 1A). The platelets also exhibit upconversion luminescence when excited by a 980-nm infrared laser. The particles were chemically treated for surface charging (see Materials and Methods), coated with a ~5-nm-thick silica layer, and then functionalized with methoxy silane polyethylene glycol (Si-PEG) (Fig. 1, B to D) (*19*). Silica capping increases the overall thickness of particles by ~10 nm, with negligible relative changes of their diameter (Fig. 1, C and D). These particles were dispersed in 4-cyano-4′-pentylbiphenyl (5CB) by mixing it with a dilute colloidal dispersion in ethanol, followed by solvent evaporation at 70°C for 2 hours and cooling down to nematic phase under rapid mechanical agitation (see Materials and Methods). The ensuing colloidal dispersions were infiltrated into ~30-μm-thick glass cells and sealed with a fast-setting epoxy glue. To promote planar boundary conditions, we coated the inner surfaces of the glass cells with polyvinyl alcohol and then rubbed them. Dispersion and alignment of particles within the LC were studied using optical microscopy (Figs. 1 to 3). Polarizing optical micrographs reveal $\mathbf{n}(\mathbf{r})$ configurations, which arise from the planar (Fig. 1, F and G), perpendicular (Fig. 1H), or conic (Fig. 1E) boundary conditions at the large-area and edge faces of the particles at different orientations relative to $\mathbf{n}_0$. The platelets respond to electric and magnetic fields in both LC and isotropic media. A magnetic field $B \approx 480$ G was used to align platelets, with their large-area faces parallel to it and $\mathbf{s} \perp \mathbf{B}$ (Fig. 1, M to P) where $\mathbf{s}$ is the normal to platelet's large-area faces.

We formed a cell using two glass substrates, with dense layers of platelets spin-coated on their inner surfaces. The nematic Schlieren texture within the infiltrated LC showed wall defects connecting half-integer disclinations (Fig. 2A), indicative of the tilted director alignment (Fig. 2B) (*21*). The measured optical phase retardation of these cells revealed a ~49° tilt of the director relative to substrates for as-purchased 5CB, which could be further controlled by ion doping. The electrostatic control of boundary conditions, which we describe in detail below for colloidal inclusions, allows tuning of boundary conditions on confining cell surfaces by coating them with these platelets or by using substrate materials with tunable surface charging.

Depending on the ionic composition within LC dispersions, platelets spontaneously orient at different angles θ between their surface normal vector $\mathbf{s}$ and $\mathbf{n}_0$ (Fig. 1J). They align with $\mathbf{s} \| \mathbf{n}_0$ when using no or <2-nm silica layer capping (Fig. 1H), inducing weak quadrupolar $\mathbf{n}(\mathbf{r})$ distortions (Fig. 1L). Freshly synthesized particles with 5-nm silica layers and Si-PEG functionalization in as-purchased 5CB (see Materials and Methods) tilt, on average, at $\theta \approx 46°$ with respect to $\mathbf{n}_0$ (Fig. 1, E, I, and J) due to their conic boundary conditions (*8*, *17*, *19*). Aging these dispersions for 1 week under ambient conditions aligns the large-area faces along $\mathbf{n}_0$, with $\theta \approx 90°$ and platelets accompanied by weak quadrupolar $\mathbf{n}(\mathbf{r})$ (Fig. 1, F, G, and K). These platelet orientations correlate with surface charging under the same conditions, which we

[1]Department of Physics and Soft Materials Research Center, University of Colorado, Boulder, CO 80309, USA. [2]Department of Electrical, Computer, and Energy Engineering, Materials Science and Engineering Program, University of Colorado, Boulder, CO 80309, USA. [3]Renewable and Sustainable Energy Institute, National Renewable Energy Laboratory, University of Colorado, Boulder, CO 80309, USA.
*Corresponding author. Email: ivan.smalyukh@colorado.edu

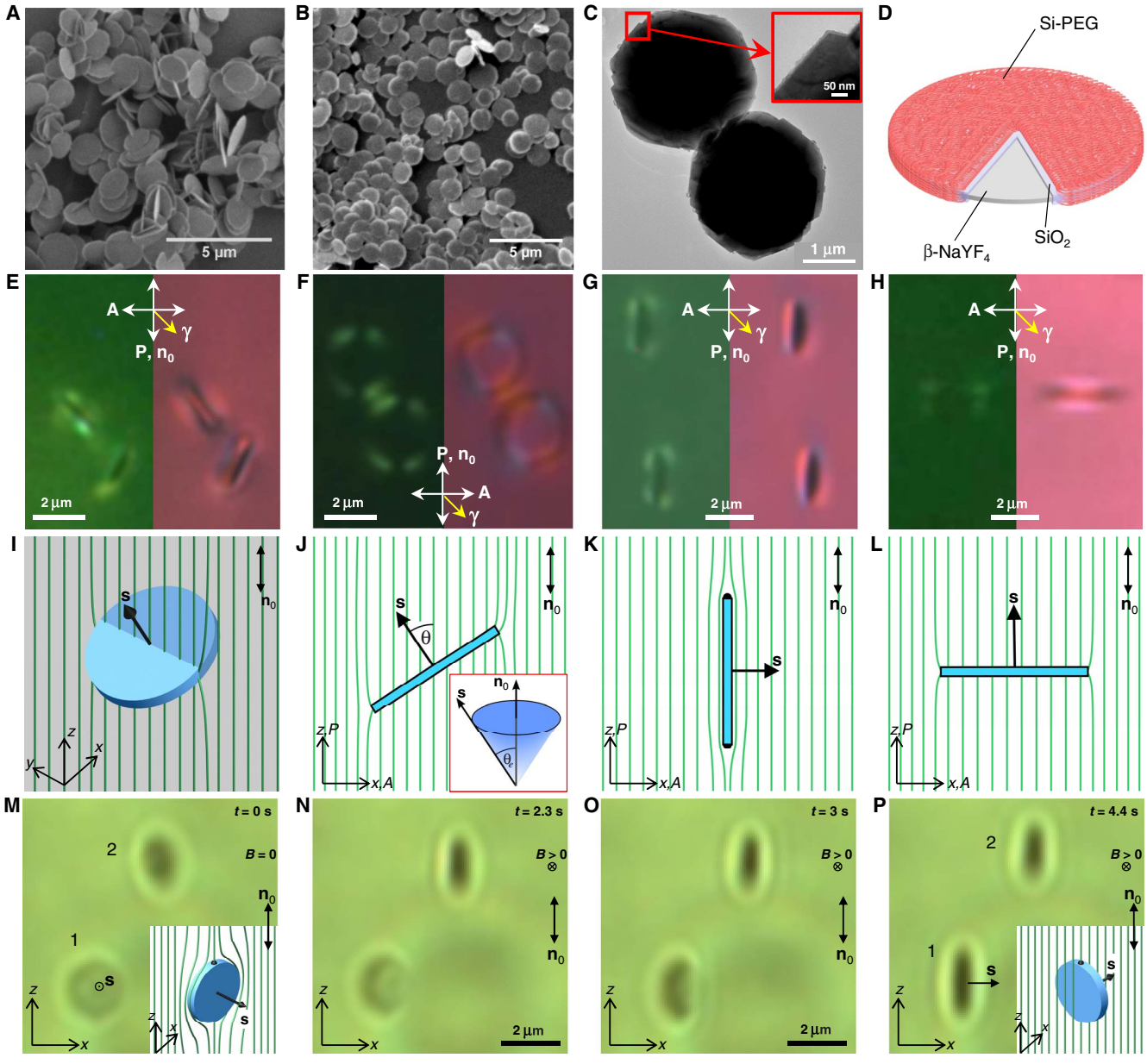

Fig. 1. Characterization of the platelets' size and orientation in nematic LC. SEM micrographs of platelets before (**A**) and after (**B**) SiO_2 coating. (**C**) TEM micrograph of particles. The inset shows the SiO_2 layer, visible at the platelet's edge as a thin gray stripe. (**D**) Schematic of the platelets showing a core, SiO_2 coating, and Si-PEG layer. (**E** to **H**) Optical micrographs of platelets with conic (E), planar (F and G), and perpendicular (H) surface anchoring under crossed polarizer P and analyzer A without (left) and with (right) a retardation plate γ in a nematic cell. (**I** to **L**) Schematic diagrams of **n**(**r**) (green lines) around platelets with conic (I and J), planar (K), and perpendicular (L) anchoring. Inset in (J) is a schematic of conic degenerate boundary conditions. (**M** to **P**) Experimental sequence of optical micrographs, with elapsed time marked, showing reorientation of platelets with planar anchoring when a magnetic field $B \approx 480$ G is applied normal to the image planes. Insets show schematics of **n**(**r**) around a platelet 1 at $\mathbf{s}\perp\mathbf{n}_0\|\mathbf{B}$ in (M) and $\mathbf{s}\perp\mathbf{n}_0\perp\mathbf{B}$ in (P).

characterize by prompting electrophoretic motion of the particles in response to an electric field applied along $\mathbf{n}_0$, followed by balancing the electrophoretic force with the viscous drag force (see Materials and Methods) (*20*). The surface charge of particles decreased from $Ze = +(200\text{-}300)e$ for as-synthesized platelets to $Ze = +(20\text{-}30)e$ for the same particles after 1-week aging, where e is the elementary charge and Z is the number of effective elementary charges. Positive surface charges and counterions in the bulk of dispersion generate the double layers with the electric field $\mathbf{E}_{DL} = -\nabla\Phi$ directed orthogonally outward from platelet's large-area faces (*24*, *25*), with magnitude quickly decreasing with distance r (Fig. 4A). This electric field couples with the director because of the bulk free energy density term $-\varepsilon_0\Delta\varepsilon E_{DL}^2(\mathbf{r})(\mathbf{s}\cdot\mathbf{n}_0)^2/2$, tending to align $\mathbf{s}\|\mathbf{n}_0$ for LCs with dielectric anisotropy $\Delta\varepsilon = \varepsilon_{||}\text{-}\varepsilon_\perp > 0$ (here, we assume purely dielectric response, although flexoelectric and surface polarization effects could also play a role), where dielectric constants $\varepsilon_{||}$ and $\varepsilon_\perp$ are measured for electric field parallel and perpendicular to the director, respectively (table S1). This coupling takes place over a distance comparable to the average Debye screening length $\bar{\xi}$ on

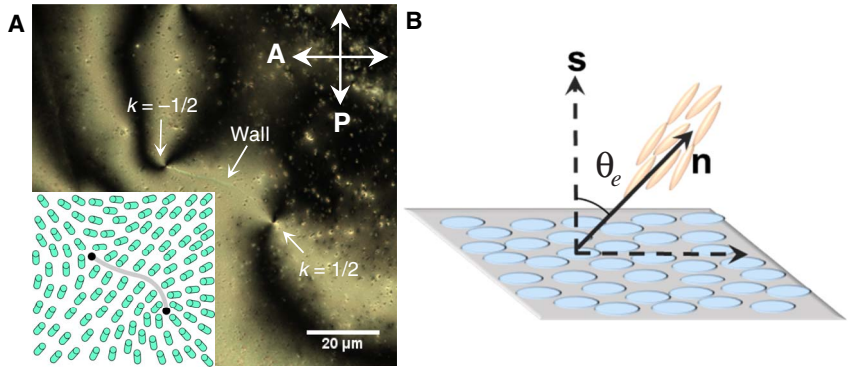

Fig. 2. Measurement of tilt angle. (**A**) Texture of a nematic LC cell with substrates covered with platelets, with conic surface anchoring caused by surface charging; the inset shows **n**(**r**) around half-integer disclinations connected by a surface wall defect, indicative of conic boundary conditions. (**B**) Corresponding schematic of LC alignment with director tilted to the surface normal **s**.

both sides of the platelet so that the electrostatic coupling energy per unit area is $W_e = -\varepsilon_0\Delta\varepsilon\cos^2\theta E_{DL}^2(\mathbf{r})\bar{\xi}$ + const. The surface anchoring energy density describing director interaction with the polymer-grafted surface in the lowest-order approximation reads $W_p = (W_1/2)\cos^2\theta + (W_2/4)\cos^4\theta$ + const (*17*). The minimum of the free energy density $W = W_p + W_e = [(W_1 - 2\varepsilon_0\Delta\varepsilon\bar{\xi}E_{DL}^2)\cos^2\theta]/2 + (W_2/4)\cos^4\theta$ + const is expected at a certain equilibrium angle θ_e dependent on the ionic content, at which $W_2 > W_1$, $(W_1 - 2\varepsilon_0\Delta\varepsilon\bar{\xi}E_{DL}^2) = W_2\cos^2\theta_e$, and $W = [(W_1 - 2\varepsilon_0\Delta\varepsilon\bar{\xi}E_{DL}^2)/(4\cos^2\theta_e)](\cos^2\theta - \cos^2\theta_e)^2$. The electrostatic contribution to W and coupling between **s** and $\mathbf{n}_0$ depend on the surface charge and ionic content of the LC, tending to orient the molecules along **s** and away from an easy axis $\mathbf{e}_p$ describing the natural coupling of the director with a Si-PEG–coated surface. Depending on grafting density, Si-PEG functionalization can give planar or conic boundary conditions (*19*). We optimize grafting to give $\mathbf{e}_p$ parallel to the platelet to obtain the entire range of tilting $\theta = 0°$ to 90° because of the aligning effect of the electric double layer. At lower surface charging, molecules align parallel to the particle surface owing to minimal electrostatic contribution to W. For high surface charging, LC molecules orient along **s**, whereas conical boundary conditions emerge at moderate charging (Fig. 4A). Experiments (Figs. 1 and 2) agree with our model predictions.

Diffusion of particles depends on the interplay of LC's anisotropic viscoelastic properties and the shape anisotropy of oriented particles (*26*, *27*). Platelets with perpendicular or planar boundary conditions distort the director and form elastic quadrupoles embedded in a uniform $\mathbf{n}_0$ background. Using video microscopy tracking of the platelets' position, we determine the diffusion coefficients according to well-established approaches (*9*, *26*, *27*). Translational diffusion of these particles is anisotropic (Fig. 3, A and B). Diffusion anisotropy is stronger for particles with planar boundary conditions ($D_{t||}/D_{t\perp} \approx 2.24$) than for particles with perpendicular anchoring ($D_{t||}/D_{t\perp} \approx 1.24$), where $D_{t||}$ and $D_{t\perp}$ are translational diffusion coefficients measured, respectively, along and perpendicular to $\mathbf{n}_0$ (*26*, *27*). Platelets with conic surface anchoring tilt with respect to $\mathbf{n}_0$ by the conic angle θ_e (Figs. 1, E and J, and 3C) and induce dipolar elastic distortions (Fig. 1, I and J). Translational diffusion of tilted particles is anisotropic ($D_{t||}/D_{t\perp} \approx 2$), but the polar plot of D_t (Fig. 3C) is rotated with respect to both $\mathbf{n}_0$ and **s**, with a typical angle between $\mathbf{n}_0$ and the direction of maximum displacement 20° to 30°. Shape anisotropy influences the diffusion of particles with planar anchoring in a homeotropic cell (Fig. 3D), which is isotropic with respect to the sample frame, but anisotropic in the particle's reference frame, being the smallest along **s**.

Platelets also experience rotational diffusion (*27*), with rotation by an angle β around $\mathbf{n}_0$ (Fig. 3D) and tilting away from the energy-minimizing orientation with respect to $\mathbf{n}_0$ by $\delta\theta = \theta - \theta_e$ (Fig. 3, A to C and E). The angular displacement in the former case is much larger than the latter, with corresponding rotational diffusion coefficients $D_{r\beta} \approx 8.2 \times 10^{-3}$ rad^2 s^{-1} and $D_{r\theta} \approx 1.5 \times 10^{-3}$ rad^2 s^{-1} estimated from histograms of the displacements $\Delta\beta$ and $\Delta\theta$ of particles like that shown in Fig. 3F (*27*), where $\Delta\beta$ and $\Delta\theta$ are the angular differences between platelet's orientations in two consecutive frames of video tracking. Figure 3G shows a rotational mean square displacement $\langle\Delta\theta^2\rangle$ of the tilted platelet (Fig. 3C) versus lag time τ, which first increases and then saturates, showing subdiffusive behavior caused by LC-mediated elastic forces. Director field perturbations due to the deviation of the particle from θ_e cost elastic free energy and generate restoring forces on the platelet, rotating it back to an equilibrium orientation. By fitting data (Fig. 3G) with $\langle\Delta\theta^2(\tau)\rangle = (k_BT/2\kappa)[1 - \exp(-4\kappa\tau/\zeta)]$ at short τ (*27*), we find the viscous rotational friction coefficient $\zeta = 6.16 \times 10^{-18}$ N m s and an orientational elastic trap stiffness $\kappa = 3.18 \times 10^{-18}$ N m, which is the energy needed to rotate a platelet out of the orientational trap set by the elastic and surface anchoring coupling and by orientation of $\mathbf{n}_0$. The probability distribution of θ (Fig. 3H) can be described by a function $f(\theta) \propto \exp[-U(\theta)/k_BT]$, where k_B is the Boltzmann constant, $T = 300$ K [3], and $U(\theta)$ is energy due to the deviation of the particle from the equilibrium orientation at θ_e. In the finite anchoring regime, $U(\theta)$ includes elastic and surface anchoring contributions (*19*)

$$U(\theta) = \frac{4\pi K(W_1 - 2\varepsilon_0\Delta\varepsilon\bar{\xi}E_{DL}^2)R^2\ \sin^2\ 2\theta_e(\theta - \theta_e)^2}{8K\ \cos^2\ \theta_e + \pi(W_1 - 2\varepsilon_0\Delta\varepsilon\bar{\xi}E_{DL}^2)R\ \sin^2\ 2\theta_e}$$

where K is an average Frank elastic constant and W_2 is the polar surface anchoring coefficient (*21*). Fitting the experimental distribution with $f(\theta)$ for radius $R = 1$ μm and $K = 7 \times 10^{-12}$ N for 5CB, we estimate $W_1 - 2\varepsilon_0\Delta\varepsilon\bar{\xi}E_{DL}^2 = (2.14 \text{ to } 5.42) \times 10^{-6}$ J m^{-2}. For studied E_{DL} and ionic contents, W_e competes with W_p only for weak coupling of $\mathbf{n}(\mathbf{r})$ to $\mathbf{e}_p$ with $W_1 \leq 10^{-5}$ J m^{-2}, as in the case of Si-PEG functionalization, for which θ_e can be varied within 0° to 90° (fig. S1). The Debye screening length for as-purchased LC hosts ranges from $\xi_\perp = 89$ nm to $\xi_{||} = 150$ nm measured for $\mathbf{s}\perp\mathbf{n}_0$ and $\mathbf{s}||\mathbf{n}_0$, respectively (table S2). For a doped LC, these values are significantly smaller: $\xi_\perp = 71$ nm and $\xi_{||} = 120$ nm (table S2). The contribution of this Debye screening length anisotropy to the angular dependence of $U(\theta)$ and its role

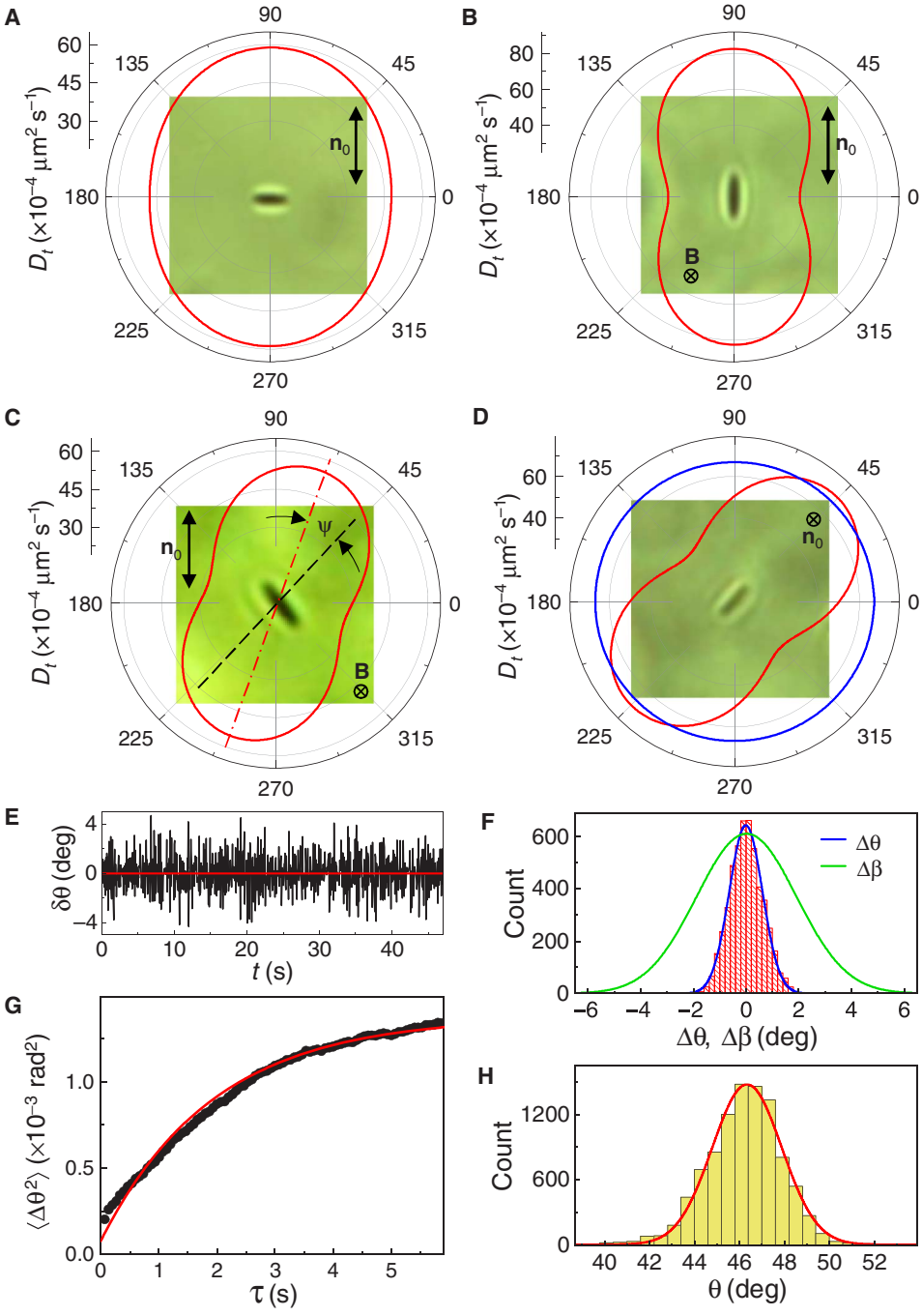

Fig. 3. Characterization of translational and rotational diffusion of platelets. Translational (**A** to **D**) and rotational (**E** to **G**) diffusion of platelets in a nematic LC. (A to C) D_t of a platelet with (A) perpendicular, (B) planar, and (C) conical boundary conditions in a planar cell with in-plane $\mathbf{n}_0$; black and red dashed lines in (C) show a normal to the platelet and a direction of maximum displacements, respectively. Magnetic field $B \approx 480$ G in (B) and (C) keeps the orientation platelet's **s** parallel to the field of view. (D) D_t of a platelet with planar surface anchoring in a homeotropic cell; red and blue plots show D_t with respect to the cell and particle coordinate frames, respectively. Inset micrographs in (A) to (D) show the actual platelets undergoing diffusion. (E) Orientational fluctuations δθ of a tilted platelet in (C) with respect to its preferred orientation θ_e versus time t obtained at $\tau = 67$ ms. (F) Histograms of angular displacements Δθ and Δβ obtained at $\tau = 67$ ms, respectively, in planar and homeotropic cells. The solid blue and green lines are Gaussian fits. (G) Angular mean square displacement $\langle\Delta\theta^2\rangle$ versus lag time τ in a planar cell. A solid red line is a fit of experimental data (black filled circles) with $\langle\Delta\theta^2(\tau)\rangle$. (**H**) Histogram of platelet orientations obtained at $\tau = 67$ ms during ~10 min.

in defining platelet orientations can be accounted for numerically (see the Supplementary Materials).

As compared to an as-purchased 5CB, ionic additives such as NaCl salt decrease $\bar{\xi}$, which increases the strength of E_{DL} within the double layers (Fig. 4A). However, doping also causes counterions to adsorb on the particle surfaces, effectively reducing the surface charge and E_{DL} (Fig. 4A). Platelets originally tilted with respect to $\mathbf{n}_0$ in an as-purchased 5CB (Fig. 4B, inset) reoriented to align large-area faces parallel to $\mathbf{n}_0$

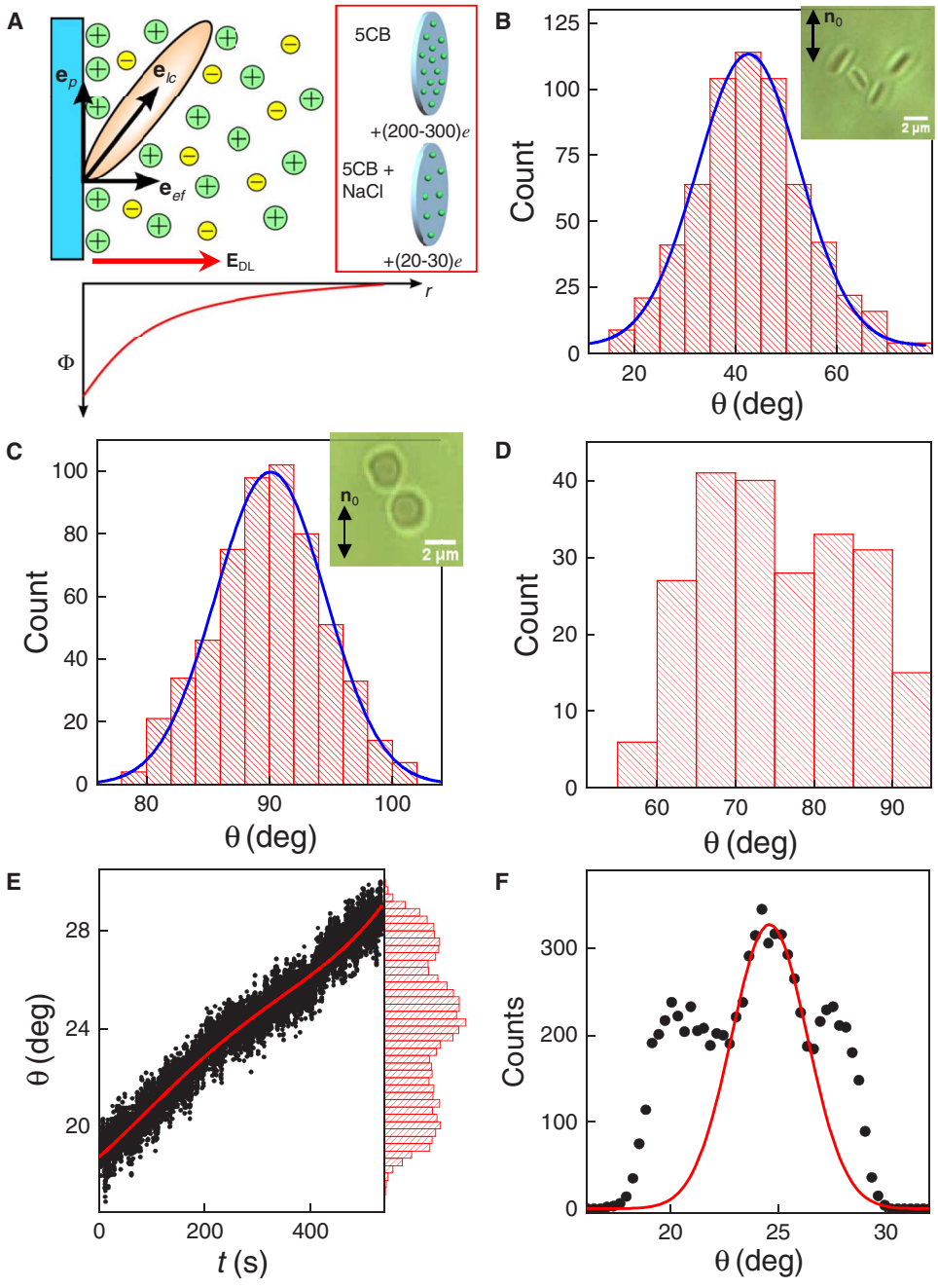

Fig. 4. Effect of ionic content of LC medium. (**A**) Schematic diagram of the LC alignment (an ellipsoid) at the surface (blue); $\mathbf{e}_p$, $\mathbf{e}_{ef}$, and $\mathbf{e}_{lc}$ show the easy axes determined by interactions with the polymer capping, electrostatic interactions, and the LC alignment resulting from their competition, respectively. Φ is an electric potential varying over the thickness of the double layer, and *r* is a distance from the platelet surface. A red arrow shows the direction of $\mathbf{E}_{DL}$. Positive and negative charges are shown by green and yellow filled circles, respectively. The right-side insets schematically show the density of a positive charge (green spheres) at the platelet surface in as-purchased and doped 5CB. (**B** to **D**) Distributions of orientation for platelets in a planar cell when dispersed in pure 5CB (B) and salt-doped 5CB for NaCl concentrations of 1 nmol/ml (C) and 0.1 nmol/ml (D). Insets in (B) and (C) are optical micrographs of platelets at orientation, tilted and parallel to $\mathbf{n}_0$ in the respective LC media. (**E**) Change of θ with time for a platelet in pure 5CB due to absorption of ions from the atmosphere. (**F**) Distributions of platelet orientations showing discrete increments in the angle θ. The red line is a Gaussian fit of the central part of a distribution shown in (E) corresponding to the completed step during the change of the orientation.

upon doping (Fig. 4C, inset). Figure 4B represents a histogram showing the variation in θ for 600 co-dispersed particles, which exhibit an average θ = 42° in pure 5CB. The same particles show planar alignment in 5CB after salt doping (1 nmol/ml), characterized by the histogram in Fig. 4C. For low-salt concentrations (~0.1 nmol/ml), particles display broad variations in θ (Fig. 4D). The measured $\xi_{||}$ of the doped LC is 120 and 140 nm for NaCl concentrations of 1 and 0.1 nmol/ml, respectively; $\xi_{\perp}$ exhibits a similar behavior (table S2). Values of $\bar{\xi}$ correlate with the LC's ionic content (tables S2 and S3). Relatively small changes of $\xi_{||}$ and $\xi_{\perp}$ compared to the dramatic change of the surface

charge per particle indicate that the main mechanism of altering boundary conditions by ionic doping is through the effective compensation of the positive charge by counterions adsorbed on particles. Figure 4E shows the rotation of the particle with respect to $\mathbf{n}_0$ due to the change of charging with time. Platelets initially aligned at $\theta_e \sim 18°$ show a gradual increase of the tilt (Fig. 4E). The distributions of the platelet orientation show several distinct peaks at different θ_e (Fig. 4, E and F), indicating that the reorientation is stepwise (Fig. 4, E and F), with platelets staying at discrete orientations for several hundred seconds before jumping to the next orientation. While this change of orientation with doping correlates with the negative counterions adsorbing to the particle surfaces and effectively neutralizing their positive charges, the detailed mechanisms of this counterion absorption for the studied particles with complex structure remain to be understood and will be explored elsewhere.

At high concentrations, platelets tend to form crystalline assemblies (Fig. 5A), owing to the competition between elastic and electrostatic interactions (*20*). The crystallographic symmetry of these colloids depends on director distortions around platelets and their charging and orientations relative to $\mathbf{n}_0$. Our results (Fig. 5) show potential for designing colloidal crystals with crystallography tunable by ion doping. We illustrate the effects of doping by probing changes of colloidal structures in a crystallographic plane parallel to cell substrates (Fig. 5), where the addition of salt alters the self-assembly. Platelets with high ~+300*e* charge have homeotropic anchoring and form a rhombic lattice (Fig. 5, A and B). When the charge decreases to ~+100*e*, and platelets adopt conic anchoring and tilt with respect to $\mathbf{n}_0$ by $\theta_e \approx 34°$, they assemble into an oblique lattice with different parameters (Fig. 5C), whereas platelets with the lowest ~+20*e* charge and planar anchoring align with **s** perpendicular to the cell substrates and also form a rhombic lattice (Fig. 5D). The two-dimensional (2D) lattices within the crystallographic planes parallel to cell substrates can be magnetically and electrically reconfigured to yield different 3D crystals by magnetically tuning platelet orientations and electrostatically varying the spacing between the crystallographic planes (*20*), although this is outside the scope of this work.

We demonstrated that the anchoring free energy and boundary conditions on colloidal particles and confining surfaces of LCs can be controlled by tuning surface charging and ionic dopant concentration. This allows the control of LC alignment with respect to the confining surfaces and the orientation of anisotropic colloidal particles, like platelets, with respect to the uniform far-field background of the LC, potentially allowing a host of reconfigurable low-symmetry crystalline and LC organizations of colloidal inclusions. Our findings expose the need of future studies of how topological defects with reduced orientational order on particle surfaces and in the LC bulk near these particles may mediate absorption of counterions and how inhomogeneous electrostatic double layers can arise from the anisotropic nature of LCs. In addition to the direct control of colloidal particle orientation through the dielectric coupling of the electric field within the double layer with LC director, future studies may also take advantage of ion absorption–mediated conformational changes within polymer molecules grafted on colloidal particles, which would modify the conventional surface anchoring. The diversity of these effects may enable means of controlling long-range order of colloidal particles in LCs that are not accessible in the conventional isotropic fluid hosts of colloidal inclusions.

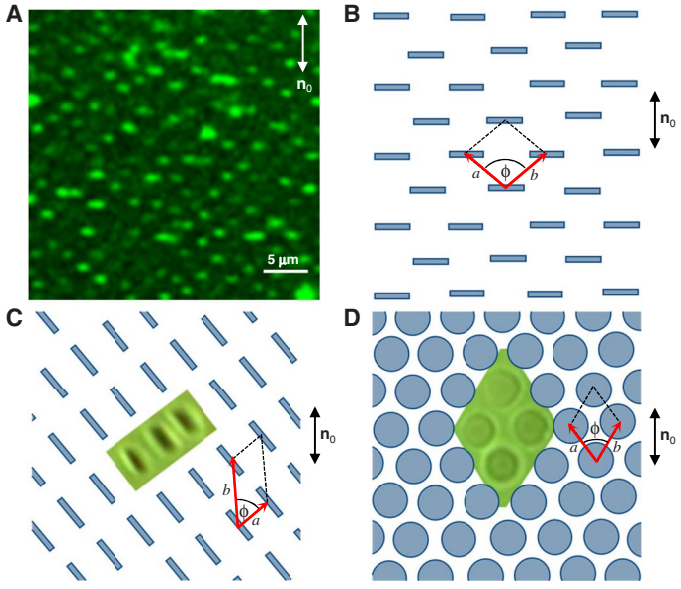

Fig. 5. Self-assembled colloidal lattice formed by platelets. (**A**) Upconversion luminescence confocal image and (**B**) schematic of a self-assembled colloidal lattice of charged platelets with perpendicular anchoring in a planar cell. The measured (defined on schematics) parameters of the rhombic lattice: $a = b \approx 3$ μm, $\phi \approx 100°$. (**C** and **D**) Schematics of 2D assemblies in a nematic LC for platelets with tilted (C) and planar (D) boundary conditions. Insets in (C) and (D) show the experimental fragments of corresponding assemblies, where $\theta_e \approx 34°$, $a \approx 2.1$ μm, $b \approx 3.7$ μm, and $\phi \approx 56°$ in (C) and $\theta_e \approx 0°$, $a = b \approx 2.5$ μm, and $\phi \approx 68°$ in (D).

MATERIALS AND METHODS

Synthesis and characterization of the colloidal platelets

The chemical ingredients used for synthesis—ytterbium nitrate hexahydrate [$Yb(NO_3)_3\,6H_2O$], yttrium nitrate hexahydrate [$Y(NO_3)_3\,6H_2O$], erbium nitrate pentahydrate [$Er(NO_3)_3\,5H_2O$], sodium fluoride (NaF), oxalic acid (OA), tetra-ethyl-orthosilicate (TEOS), and polyvinyl pyrrolidone (PVP; M_w: 40 kDa)—were all purchased from Sigma-Aldrich. Sodium hydroxide (NaOH) was purchased from Alfa Aesar, and Si-PEG (M_w: 5 kDa) was purchased from JenKem Technology.

We synthesized β-$NaYF_4$:Yb,Er platelets by following a hydrothermal synthesis method (*23*). Briefly, 0.7 g of NaOH was dissolved in 20 ml of deionized water, and 1.102 g of OA was added at room temperature under vigorous stirring. After obtaining a clear solution, 202 mg of NaF was added to the mixture and kept stirring for another 15 min. Then, 1.1 ml of $Y(NO_3)_3$ (0.8 M), 0.35 ml of $Yb(NO_3)_3$ (0.63 M), and 0.05 ml of $Er(NO_3)_3$ (0.4 M) were injected into the solution and kept stirring for another 20 min. The mixture was transferred to a Teflon-lined autoclave and kept in an oven at temperature 200°C for 12 hours. After the reaction, the solution was allowed to cool down to room temperature naturally, and the particles were collected from the bottom of the Teflon chamber, washed with deionized water multiple times, and finally dispersed in 10 ml of deionized water. The reaction yields circular plates with an average diameter of 2 μm and a thickness of ~20 nm. For further surface treatment, 1 ml of particle dispersion was mixed with 5 ml of hydrogen peroxide and 100 μl of nitric acid and kept stirring for overnight. This process ensures complete removal of the OA from the particle surface, leaving the particle positively charged. The uncapped platelets were precipitated from the solution by centrifugation and finally dispersed in 1 ml of ethanol. Then, the

platelets were covered with a thin layer of silica (SiO_2). For this process, 300 mg of PVP was dissolved in 4 ml of ethanol by ultrasonification, and 1 ml of the platelet dispersion in ethanol was mixed with this solution and kept stirring for 24 hours. The PVP ligands adsorbed to the particle surface, which favored silica growth at the particle surface. The PVP-coated particles were separated from the solution by centrifugation and redispersed in 5 ml of ethanol. Then, 250 μl of ammonia solution (28 weight % in water) was added to the dispersion, followed by 8 μl of TEOS with continuous agitation for 12 hours. The dispersions of silica-coated particles were centrifuged at 6000 rpm for 5 min and redispersed in 5 ml of ethanol. Then, 2 ml of ammonia solution was added to the mixture, bringing the pH of the solution ~12, which was immediately followed by adding 1 ml of hot Si-PEG solution in ethanol (25 mg/ml) under constant agitation. After 12 hours, the Si-PEG functionalized particles were precipitated by centrifugation, washed with deionized water multiple times, and redispersed in 1 ml of ethanol for subsequent use. The synthesis conditions mentioned above resulted in SiO_2 thickness of 5 nm, but the thickness of the SiO_2 layer can be tuned by varying the concentration of TEOS in the reaction. The particle size, polydispersity, and thickness of the SiO_2 layer were characterized using transmission electron microscopy (TEM; FEI Tecnai T12) and SEM (FEI Quanta 600) images of the particles. The samples for TEM and SEM characterization were prepared by drop casting a dilute dispersion of the particles in ethanol onto a carbon-coated copper grid and silicon substrate, respectively, and dried under an inert atmosphere. To disperse the particles in LC, a dilute solution of particle dispersion in ethanol was mixed with 13 μl of 5CB, followed by heating at 70°C for 2 hours for ethanol evaporation. Then, the mixture was rapidly cooled down to the nematic phase under rapid mechanical agitation. The optical microscopy images of the particles were collected using a color charge-coupled device camera (Flea-col, Point Grey) attached to an inverted microscope (IX 81, Olympus). The microscope is equipped with objective lenses with magnifications of ×10, ×50, ×60, and ×100 and polarizing filters to control the polarization state of the illumination light.

Surface charge estimation

The surface charge of the particles was estimated from the electrophoretic motion of a single particle dispersed in 5CB (table S1). When subjected to an external electric field E_{ext}, the positively charged particles moved in the direction of field lines and the surface charge of the particles can be estimated from the balance of Stokes drag force $F_S = \zeta_s v$ and electrostatic force $F_e = ZeE_{ext}$, where ζ_s is the viscous friction coefficient, v is the velocity of the particle in 5CB, $e = 1.6 \times 10^{-19}$ C is the elementary charge, and Z is the effective number of elementary charges at the particle surface. The velocity v of the particles was estimated from the displacement of the particle when subjected to an external electric field $E_{ext} = 10^4$ V/m. The friction coefficient ζ_s of the particles was estimated from the particle's diffusion constant D in the medium using the Einstein relation $\zeta_s D = k_B T$, where k_B is the Boltzmann constant and T is an absolute temperature. The diffusion constant D of the particles was calculated from distributions of the particle displacements for a fixed time interval during the Brownian motion in the LC medium. The measured surface charge on the uncapped platelets was ~+300e. The process of silica capping reduced the effective surface charge on the particles to +(100-200)e, indicating that the charging on the particles is dominated by the positively charged cores of the particles, although it can also be controlled by silica coating.

Estimation of the Debye screening length of the LC medium

The Debye screening length depends on dielectric constants of the LC medium (table S1). For example, it ranges from $\xi_\perp = 89$ nm to $\xi_{||} = 150$ nm when measured for $\mathbf{s}\perp\mathbf{n}_0$ and $\mathbf{s}||\mathbf{n}_0$, respectively, for an as-purchased LC host (table S2). This anisotropy was preserved upon aging or doping of the LC with ions, although the values of $\xi_\perp$ and $\xi_{||}$ change considerably (tables S2 and S3). This anisotropic orientation-dependent Debye screening length strongly depends on the effective dielectric constant of the LC that, in turn, depends on the orientation of electric field and platelet's normal relative to the LC director: $\xi(\theta) = [(\varepsilon_\perp + \Delta\varepsilon\cos^2\theta_e)\varepsilon_0 k_B T/2N_A e^2 I]^{1/2}$, where N_A is the Avogadro's number and I is the ionic concentration determined by measuring conductivity. Along with the orientation-dependent dielectric constant $\varepsilon(\theta) = \varepsilon_\perp + \Delta\varepsilon\cos^2\theta$ (table S1), anisotropy of the Debye screening length also contributes to the angular dependence of the electric field of the double layer $\mathbf{E}_{DL} = -\nabla\Phi = -\nabla\{(Ze/[2\pi R^2\varepsilon_0\varepsilon(\theta_e)])\exp[-r/\xi(\theta_e)]$. To estimate values of the Debye screening length at different conditions, the ionic concentration I of as-purchased 5CB and NaCl-doped 5CB was calculated from the conductivity C of the sample following the Walden's rule (*28*). Using the literature values of equivalent conductance of hydrochloric acid (HCl) in ethanol, this can be written as $\Lambda^{LC}\eta^{LC} = \Lambda^E\eta^E$, where Λ^{LC} and Λ^E are the equivalent conductance of 5CB and ethanol, and η^{LC} and η^E represent the viscosity values of 5CB and ethanol. The ionic concentration is $I = C/\Lambda^{LC}$. The conductivity C of the LC host was calculated from the measured values of the current passing through the sample by applying a low-frequency voltage (10 V, 1 Hz) between the electrodes of the LC cell. Tables S2 and S3 summarize the estimated values of $\xi_{||}$, $\xi_\perp$, and I for NaCl-doped 5CB and as-purchased 5CB, indicating the variations of the Debye screening length with salt concentration and elapsed time after cell preparation.

SUPPLEMENTARY MATERIALS

Supplementary material for this article is available at http://advances.sciencemag.org/cgi/content/full/5/9/eaax4257/DC1

Supplementary Text

Table S1. Physical parameters of 5CB.

Table S2. Variations of Debye screening with ionic concentration.

Table S3. Variations of Debye screening with time.

Fig. S1. Variation of equilibrium conic angle and angular distribution with surface charge on the platelets.

REFERENCES AND NOTES

1. Z. Dogic, P. Sharma, M. J. Zakhary, Hypercomplex liquid crystals. *Annu. Rev. Condens. Matter Phys.* **5**, 137–157 (2014).
2. S. J. Woltman, G. D. Jay, G. P. Crawford, Liquid-crystal materials find a new order in biomedical applications. *Nat. Mater.* **6**, 929–938 (2007).
3. P. M. Chaikin, T. C. Lubensky, *Principles of Condensed Matter Physics* (Cambridge Univ. Press, 1995).
4. P. Poulin, H. Stark, T. C. Lubensky, D. A. Weitz, Novel colloidal interactions in anisotropic fluids. *Science* **275**, 1770–1773 (1997).
5. H. Stark, Physics of colloidal dispersions in nematic liquid crystals. *Phys. Rep.* **351**, 387–474 (2001).
6. T. C. Lubensky, D. Pettey, N. Currier, H. Stark, Topological defects and interactions in nematic emulsions. *Phys. Rev. E* **57**, 610–625 (1998).
7. I. I. Smalyukh, Liquid crystal colloids. *Annu. Rev. Condens. Matter Phys.* **9**, 207–226 (2018).
8. B. Senyuk, O. Puls, O. M. Tovkach, S. B. Chernyshuk, I. I. Smalyukh, Hexadecapolar colloids. *Nat. Commun.* **7**, 10659 (2016).
9. C. P. Lapointe, T. G. Mason, I. I. Smalyukh, Shape-controlled colloidal interactions in nematic liquid crystals. *Science* **326**, 1083–1086 (2009).
10. B. Senyuk, Q. Liu, E. Bililign, P. D. Nystrom, I. I. Smalyukh, Geometry-guided colloidal interactions and self-tiling of elastic dipoles formed by truncated pyramid particles in liquid crystals. *Phys. Rev. E* **91**, 040501 (2015).

11. F. Brochard, P. G. de Gennes, Theory of magnetic suspensions in liquid crystals. *J. Phys.* **31**, 691–708 (1970).
12. T. A. Wood, J. S. Lintuvuori, A. B. Schofield, D. Marenduzzo, W. C. K. Poon, A self-quenched defect glass in a colloid-nematic liquid crystal composite. *Science* **334**, 79–83 (2011).
13. A. Mertelj, D. Lisjak, M. Drofenik, M. Čopič, Ferromagnetism in suspensions of magnetic platelets in liquid crystal. *Nature* **504**, 237–241 (2013).
14. J. S. Evans, C. N. Beier, I. I. Smalyukh, Alignment of high-aspect ratio colloidal gold nanoplatelets in nematic liquid crystals. *J. Appl. Phys.* **110**, 033535 (2011).
15. N. M. Silvestre, M. Tasinkevych, Key-lock colloids in a nematic liquid crystal. *Phys. Rev. E* **95**, 012606 (2017).
16. J. Dontabhaktuni, M. Ravnik, S. Žumer, Quasicrystalline tilings with nematic colloidal platelets. *Proc. Natl. Acad. Sci. U.S.A.* **111**, 2464–2469 (2014).
17. O. O. Ramdane, P. Auroy, S. Forget, E. Raspaud, P. Martinot-Lagarde, I. Dozov, Memory-free conic anchoring of liquid crystals on a solid substrate. *Phys. Rev. Lett.* **84**, 3871–3874 (2000).
18. H. Mundoor, S. Park, B. Senyuk, H. H. Wensink, I. I. Smalyukh, Hybrid molecular-colloidal liquid crystals. *Science* **360**, 768–771 (2018).
19. Q. Liu, P. J. Ackerman, T. C. Lubensky, I. I. Smalyukh, Biaxial ferromagnetic liquid crystal colloids. *Proc. Natl. Acad. Sci. U.S.A.* **113**, 10479–10484 (2016).
20. H. Mundoor, B. Senyuk, I. I. Smalyukh, Triclinic nematic colloidal crystals from competing elastic and electrostatic interactions. *Science* **352**, 69–73 (2016).
21. P. G. de Gennes, J. Prost, *The Physics of Liquid Crystals* (Oxford Univ. Press, ed. 2, 1993).
22. Y. Yuan, G. N. Abuhaimed, Q. Liu, I. I. Smalyukh, Self-assembled nematic colloidal motors powered by light. *Nat. Commun.* **9**, 5040 (2018).
23. J. Yang, D. Shen, X. Li, W. Li, Y. Fang, Y. Wei, C. Yao, B. Tu, F. Zhang, D. Zhao, One-step hydrothermal synthesis of carboxyl-functionalized upconversion phosphors for bioapplications. *Chemistry* **18**, 13642–13650 (2012).
24. R. R. Shah, N. L. Abbott, Coupling of the orientations of liquid crystals to electrical double layers formed by the dissociation of surface-immobilized salts. *J. Phys. Chem. B* **105**, 4936–4950 (2001).
25. A. Poniewierski, T. J. Sluckin, Statistical mechanics of a simple-model of the nematic liquid crystal. 2. *Mol. Cryst. Liq. Cryst.* **126**, 143–160 (1985).
26. J. C. Loudet, P. Hanusse, P. Poulin, Stokes drag on a sphere in a nematic liquid crystal. *Science* **306**, 1525 (2004).
27. B. Senyuk, D. Glugla, I. I. Smalyukh, Rotational and translational diffusion of anisotropic gold nanoparticles in liquid crystals controlled by varying surface anchoring. *Phys. Rev. E* **88**, 062507 (2013).
28. C. P. Royall, M. E. Leunissen, A. van Blaaderen, A new colloidal model system to study long-range interactions quantitatively in real space. *J. Phys. Condens. Matter* **15**, S3581–S3596 (2003).

Acknowledgments: We thank N. Abbott and Q. Liu for discussions. **Funding:** This work was supported by Department of Energy, Office of Basic Energy Sciences, under award ER46921, contract DE-SC0019293 with University of Colorado Boulder. **Author contributions:** H.M., B.S., M.A., S.P., and B.F. synthesized the platelets and performed the experiments. I.I.S. conceived and directed the project. H.M., B.S., and I.I.S. analyzed the results and wrote the manuscript with input from all authors. **Competing interests:** The authors declare that they have no competing interests. **Data and materials availability:** All data needed to evaluate the conclusions in the paper are present in the paper and/or the Supplementary Materials. Additional data related to this paper may be requested from the authors.

Submitted 21 March 2019
Accepted 23 August 2019
Published 20 September 2019
10.1126/sciadv.aax4257

Citation: H. Mundoor, B. Senyuk, M. Almansouri, S. Park, B. Fleury, I. I. Smalyukh, Electrostatically controlled surface boundary conditions in nematic liquid crystals and colloids. *Sci. Adv.* **5**, eaax4257 (2019).

Science Advances

Electrostatically controlled surface boundary conditions in nematic liquid crystals and colloids

Haridas Mundoor, Bohdan Senyuk, Mahmoud Almansouri, Sungoh Park, Blaise Fleury and Ivan I. Smalyukh

Sci Adv **5** (9), eaax4257.
DOI: 10.1126/sciadv.aax4257